Mercury's moment of inertia from spin and gravity data

Jean-Luc Margot,[1,2] Stanton J. Peale,[3] Sean C. Solomon,[4,5] Steven A. Hauck II,[6] Frank D. Ghigo,[7] Raymond F. Jurgens,[8] Marie Yseboodt,[9] Jon D. Giorgini,[8] Sebastiano Padovan,[1] and Donald B. Campbell[10]

[1]   Earth-based radar observations of the spin state of Mercury at 35 epochs between 2002 and 2012 reveal that its spin axis is tilted by (2.04 ± 0.08) arc min with respect to the orbit normal. The direction of the tilt suggests that Mercury is in or near a Cassini state. Observed rotation rate variations clearly exhibit an 88-day libration pattern which is due to solar gravitational torques acting on the asymmetrically shaped planet. The amplitude of the forced libration, (38.5 ± 1.6) arc sec, corresponds to a longitudinal displacement of $\sim$450 m at the equator. Combining these measurements of the spin properties with second-degree gravitational harmonics (Smith et al., 2012) provides an estimate of the polar moment of inertia of Mercury $C/MR^2 = 0.346 \pm 0.014$, where M and R are Mercury's mass and radius. The fraction of the moment that corresponds to the outer librating shell, which can be used to estimate the size of the core, is $C_m/C = 0.431 \pm 0.025$.

1.   Introduction

[2]   Bulk mass density $\rho = M/V$ is the primary indicator of the interior composition of a planetary body of mass M and volume V. To quantify the structure of the interior, the most useful quantity is the polar moment of inertia

$$C = \int_V \rho(x,y,z)(x^2 + y^2)dV. \qquad (1)$$

In this volume integral expressed in a cartesian coordinate system with principal axes $\{x, y, z\}$, the local density is multiplied by the square of the distance to the axis of rotation, which is assumed to be aligned with the z axis. Moments of inertia computed about the equatorial axes x and y are denoted by A and B, with $A < B < C$. The moment of inertia (MoI) of a sphere of uniform density and radius R is $0.4\ MR^2$. Earth's polar MoI value is $0.3307\ MR^2$ [*Yoder*, 1995], indicating a concentration of denser material toward the center, which is recognized on the basis of seismological and geochemical evidence to be a primarily iron-nickel core extending $\sim$55% of the planetary radius. The value for Mars is $0.3644\ MR^2$, suggesting a core radius of $\sim$50% of the planetary radius [*Konopliv et al.*, 2011]. The value for Venus has never been measured. Here we describe our determination of the MoI of Mercury and that of its outer rigid shell (C_m), both of which can be used to constrain models of the interior [*Hauck et al.*, 2007; *Riner et al.*, 2008; *Rivoldini et al.*, 2009].

[3]   Both the Earth and Mars polar MoI values were secured by combining measurements of the precession of the spin axis due to external torques (Sun and/or Moon), which depends on $[C - (A + B)/2]/C$, and of the second-degree harmonic coefficient of the gravity field $C_{20} = -[C - (A + B)/2]/(MR^2)$. Although this technique is not applicable at Mercury, *Peale* [1976] proposed an ingenious procedure to estimate the MoI of Mercury and that of its core based on only four quantities. The two quantities related to the gravity field, C_{20} and $C_{22} = (B - A)/(4MR^2)$, have been determined to better than 1% precision by tracking of the MESSENGER spacecraft [*Smith et al.*, 2012]. The two quantities related to the spin state are the obliquity θ (tilt of the spin axis with respect to the orbit normal) and amplitude of forced libration in longitude γ (small oscillation in the orientation of the long axis of Mercury relative to uniform spin). They have been measured by Earth-based radar observations at 18 epochs between 2002 and 2006. These data provided strong observational evidence that the core of Mercury is molten, and that

[1]Department of Earth and Space Sciences, University of California, Los Angeles, California, USA.
[2]Department of Physics and Astronomy, University of California, Los Angeles, California, USA.
[3]Department of Physics, University of California, Santa Barbara, California, USA.
[4]Department of Terrestrial Magnetism, Carnegie Institution of Washington, Washington, D. C., USA.
[5]Lamont-Doherty Earth Observatory, Columbia University, Palisades, New York, USA.
[6]Department of Earth, Environmental, and Planetary Sciences, Case Western Reserve University, Cleveland, Ohio, USA.
[7]National Radio Astronomy Laboratory, Green Bank, West Virginia, USA.
[8]Jet Propulsion Laboratory, Pasadena, California, USA.
[9]Royal Observatory of Belgium, Uccle, Belgium.
[10]Department of Astronomy, Cornell University, Ithaca, New York, USA.

Corresponding author: J.-L. Margot, Department of Earth and Space Sciences, University of California, 595 Charles Young Dr. E., Los Angeles, CA 90095, USA. (jlm@ess.ucla.edu)

Figure 1. Radar echoes from Mercury sweep over the surface of the Earth during the 2002 May 23 observations. Diagrams show the trajectory of the speckles one hour (left) before, (middle) during, and (right) one hour after the epoch of maximum correlation. Echoes from two receive stations (red triangles) exhibit a strong correlation when the antennas are suitably aligned with the trajectory of the speckles (green dots shown with a 1 s time interval).

Mercury occupies Cassini state 1 [*Margot et al.*, 2007]. Here we extend the baseline of observations to a total of 35 epochs spanning 2002–2012, and we provide improved estimates of θ, γ, C, and C_m.

2. Methods

2.1. Formalism

[4] *Peale* [1969, 1988] has shown that a simple relationship exists between obliquity, gravity harmonics, and C/MR^2 for bodies in Cassini state 1:

$$K_1(\theta)C_{20}\left(\frac{MR^2}{C}\right) + K_2(\theta)4C_{22}\left(\frac{MR^2}{C}\right) = K_3(\theta), \qquad (2)$$

where the functions $K_{1,2,3}$ depend only on obliquity and known ancillary quantities (orbital inclination and precession rate with respect to the Laplace pole). Equation (2) or one of its explicit variants can be used to determine Mercury's MoI C/MR^2 if the obliquity θ and gravity coefficients C_{20} and C_{22} are known. By far the largest source of uncertainty in estimating the MoI comes from measurements of the obliquity θ. Errors on the determination of ancillary quantities contribute to the uncertainty at the percent level [*Yseboodt and Margot*, 2006]. Residual uncertainties in the knowledge of the gravity harmonics [*Smith et al.*, 2012] contribute at less than the percent level.

[5] *Peale* [1976, 1988] also showed that observations of the forced libration in longitude, which results from torques by the Sun on the asymmetric figure of the planet, can inform us about the MoI of the outer rigid shell C_m (or, equivalently, that of the core $C_c = C - C_m$). This is because the magnitude of the torque and the amplitude of the libration are both proportional to $(B - A)/C_m$. The MoI of the outer rigid shell is obtained by writing the identity

$$\frac{C_m}{C} = 4C_{22}\left(\frac{MR^2}{C}\right)\left(\frac{C_m}{B-A}\right). \qquad (3)$$

[6] The four quantities identified by *Peale* [1976] can be used to probe the interior structure of the planet. The gravitational harmonics C_{20} and C_{22} are combined with the obliquity θ in equation (2) to yield C/MR^2. This also yields C, since M and R are known. The amplitude of the forced libration provides the quantity $(B - A)/C_m$, which is used with previous quantities in equation (3) to yield C_m/C. This in turn yields C_m and C_c. Models of the interior must satisfy the MoI values for the core (C_c) and for the entire planet (C).

2.2. Observational Technique

[7] The gravity measurements are described elsewhere [*Smith et al.*, 2012]. Here we focus on measurements of the spin state, especially the obliquity and amplitude of forced libration. The spin state can be characterized to high precision with an Earth-based radar technique that relies on the theoretical ideas of *Holin* [1988, 1992]. He showed that radar echoes from solid planets can display a high degree of correlation when observed by two receiving stations with appropriate positions in four-dimensional space-time. Normally each station observes a specific time history of fluctuations in the echo power (also known as *speckles*), and the signals recorded at separate antennas do not correlate. But during certain times on certain days of the year, the antennas become suitably aligned with the speckle trajectory, which is tied to the rotation of the observed planet (Figure 1). During these brief (∼10–20 s) time intervals a cross-correlation of the two echo time series yields a high score at a certain value of the time lag (∼5–10 s). The *epoch* at which the high correlation occurs provides a strong constraint on the orientation of the spin axis. The *time lag* at which the high correlation occurs provides a direct measurement of the spin rate.

[8] A practical implementation of the technique was developed by *Margot et al.* [2007]. We illuminate the planet with monochromatic radiation (8560 MHz, 450 kW) from the Deep Space Network (DSN) 70 m antenna in Goldstone, California (DSS-14), and we record the speckle pattern as it sweeps over two receiving stations (DSS-14 and the 100 m antenna in Green Bank, West Virginia). The transmitted waveform is circularly polarized (right-circular, IEEE definition), and we record the echoes in both right-circular (same sense, SC) and left-circular polarizations (opposite

sense, OC). To compensate for the Earth-Mercury Doppler shift, the transmitted waveform is continuously adjusted in frequency (by up to ~2.5 MHz) so that the echo center at the Green Bank Telescope (GBT) remains fixed at 8560 MHz. Because the Doppler is compensated for the GBT, there is a residual Doppler shift during reception at Goldstone. Differential Doppler corrections are performed by a programmable local oscillator at the DSN so that the echo center also remains fixed in frequency. We apply a number of frequency downconversion, filtering, and amplification operations to the signal. During conversion to baseband the in-phase (I) and quadrature (Q) components of the signal are generated. Both are sampled at 5 MHz by our custom-built data-taking systems (http://www2.ess.ucla.edu/~jlm/research/pfs) and stored on a computer storage medium for subsequent processing.

2.3. Data Reduction Technique

[9] After the observations we downsample our data to effective sampling rates f_s between 200 Hz and 5000 Hz and compute the complex cross-correlation of the DSN and GBT signals (Appendix A). This is a two-dimensional correlation function in the variables epoch t and time lag τ. Examples of one-dimensional slices through the peak of the correlation function are shown in Figure 1 of *Margot et al.* [2007]. We fit Gaussians to the one-dimensional slices to obtain estimates of the epoch of correlation maximum $\hat{t}$ and of the time lag $\hat{\tau}$ that maximizes the correlation.

[10] For epoch correlations, we typically use f_s = 200 Hz, about half the Doppler broadening due to Mercury's rotation, and integration times of 1–2 s. The one-standard-deviation widths of the Gaussians are used as nominal epoch uncertainties, with or without $1/\sqrt{\text{SNR}}$ scaling, where SNR is signal-to-noise ratio (Appendix A).

[11] For time lag correlations, we typically use f_s = 1000–5000 Hz and integration times of 1 s, yielding ~10–20 independent estimates during the high correlation period. These estimates vary noticeably with time but display a high degree of consistency, which allows us to remove obvious outliers. We perform a linear regression on the remaining estimates and report the time lag $\hat{\tau}$ corresponding to the epoch of correlation maximum $\hat{t}$. The root-mean square scatter about the regression line is used as an estimate of the time lag uncertainty.

2.4. Spin State Estimates

[12] The observables $\hat{t}$ and $\hat{\tau}$ are used to provide spin state estimates (spin axis orientation and instantaneous spin rates). In these calculations the planet state vectors are furnished by the Jet Propulsion Laboratory Planetary Ephemeris DE421 [*Folkner et al.*, 2008], and the Earth orientation is provided by the latest timing and polar motion data. The formalism for predicting the (t, τ) values that yield high correlations is described in Appendix B. We link the observables $\hat{t}$ and $\hat{\tau}$ to spin state estimates using these predictions with the following procedures.

[13] The space-time positions of the two receiving stations at the epochs of correlation maxima are used to solve for the spin axis orientation that generates similar speckles at both receiving stations. We use a least-squares approach to minimize the residuals between the predicted epochs and the

observed epochs. Various subsets of epoch measurements are combined to identify the best-fit spin axis orientation referred to the epoch J2000. The precession model for the spin axis is based on the assumption that the orbital precession rates are applicable, which is expected if Mercury closely follows the Cassini state. The orbital precession values are taken from *Margot* [2009] and amount to a precession of ~0.1 arc min over the 10-year observation interval.

[14] Once the spin axis orientation is determined, each time lag measurement is used to determine the instantaneous spin rate at the corresponding epoch, once again based on the similarity requirement for the speckles. We iteratively adjust the nominal spin rate of 6.1385025 deg/day by a multiplicative factor until the predicted time lag matches the observed time lag. A correction factor for refraction within Earth's atmosphere is applied to the spin rate at each observation epoch (Appendix C).

[15] The nominal DSN-GBT baseline is 3,260 km in length. In the spin rate problem, it is the projected baseline that is relevant, i.e., the baseline component that is perpendicular to the line of sight. Because of the displacement of the light rays due to refraction in the atmosphere, the effective projected baseline differs from the nominal value. The worst case correction at the largest zenith angle of ~84° is ~150 m for a projected baseline of ~1200 km, i.e., a fractional change of ~1 part in 10,000. Because corrections are substantial only at very large zenith angles, the majority of our observations are not affected significantly by atmospheric refraction.

3. Spin State

3.1. Observational Circumstances

[16] Between 2002 and 2012 we secured 58 sessions at the DSN and GBT telescopes (out of a larger number of sessions requested). Of those, 21 sessions were not successful. The lost sessions at Goldstone were due to pointing problems (5), failure of the motor-generator (5), heat exchanger problems (2), a defective filament power supply (1), failure of the quasi-optical mirror (1), a defective data-taking system (1), sudden failure of the transmitter (1), and operator error (2). The lost tracks at GBT were due to repair work on the azimuth track (2) and pointing (1). The remaining 37 sessions were successful, but the data from two sessions near superior conjunction are of low quality and were not used in the analysis. Thus, data from 35 sessions obtained in a 10-year interval are presented in this paper, which roughly doubles the number of sessions (18) and time span (4 years) of our previous analysis [*Margot et al.*, 2007].

[17] The observational circumstances of the 35 sessions are listed in Table 1. The round-trip light time (RTT) to Mercury strongly affects the SNR ($\propto \text{RTT}^{-4}$). The antenna elevation angles dictate the magnitude of the refraction corrections. Refraction effects lengthen the effective distance (the projected baseline) that the speckles travel during the measured time lag, which results in an increase in the spin rate that would have otherwise been determined. The range of ecliptic longitudes of the projected baselines indicates that we have observed Mercury with a variety of baseline orientations, which is important for a secure determination of the spin axis orientation.

Table 1. Observational Circumstances[a]

No.	Date (yymmdd)	RTT (s)	el$_{DSN}$ (deg)	el$_{GBT}$ (deg)	Refract (δ)	B$_{proj}$ (km)	B$_{long}$ (deg)
01	020513	659.5	76.8	50.0	0.0062	2977.0	160.1
02	020522	563.2	73.0	45.8	0.0075	2879.1	158.1
03	020602	566.9	66.2	38.3	0.0119	2658.0	152.0
04	020612	674.4	65.7	38.1	0.0120	2661.4	151.5
05	030113	668.1	32.4	30.5	0.0121	3254.6	18.4
06	030123	789.7	32.4	28.3	0.0133	3235.0	12.2
07	030531	776.1	53.3	24.2	0.0432	2084.6	135.4
08	030601	793.0	54.1	25.0	0.0395	2121.2	136.3
09	040331	826.3	52.4	23.0	0.0505	2016.4	120.2
10	041212	687.0	30.2	8.9	0.1587	2380.1	−15.1
11	041218	776.0	29.8	7.0	0.2672	2210.7	−19.8
12	041219	796.4	29.8	7.0	0.2678	2209.6	−19.9
13	050314	876.7	38.6	9.1	0.5001	1342.6	101.7
14	050315	850.1	39.5	10.1	0.4031	1390.1	102.5
15	050316	798.9	40.9	11.5	0.2973	1462.0	103.6
16	050318	751.7	41.7	12.3	0.2529	1502.1	104.2
17	060629	688.3	37.6	64.0	0.0121	2687.6	−149.8
18	060712	576.4	30.9	58.0	0.0199	2463.3	−151.3
19	080705	923.3	71.9	62.4	0.0040	3233.7	172.6
20	080706	945.7	71.1	63.8	0.0040	3244.2	173.9
21	090112	775.5	24.4	34.1	0.0172	3117.6	37.4
22	090113	753.6	24.5	34.4	0.0171	3116.4	37.1
23	090114	733.4	24.7	34.5	0.0168	3118.0	36.6
24	090619	945.4	71.1	44.9	0.0080	2874.4	156.1
25	100102	681.6	32.8	27.6	0.0138	3220.8	16.6
26	100103	674.8	33.1	27.3	0.0140	3210.7	15.3
27	100110	706.7	34.4	24.9	0.0167	3127.4	7.1
28	110415	582.5	36.8	7.3	0.8053	1235.6	105.2
29	110416	586.5	35.9	6.4	1.0544	1186.8	104.6
30	120313	707.1	36.6	7.1	0.8523	1234.5	96.7
31	120314	688.4	36.4	6.9	0.8945	1225.1	96.4
32	120315	671.5	36.1	6.6	0.9814	1207.4	96.0
33	120702	803.2	30.6	58.4	0.0218	2410.1	−143.3
34	120703	788.0	29.2	57.1	0.0247	2353.6	−142.5
35	120704	773.0	27.8	55.9	0.0282	2297.2	−141.7

[a]Each row gives the session number, the UT date of observation, the round-trip light time (RTT), the elevation angles at DSN and GBT during reception, the correction factor (α) required to account for refraction in the atmosphere (expressed as $\delta = (\alpha - 1) \times 1000$), the length of the projected baseline, and the ecliptic longitude of the projected baseline.

3.2. Epoch and Time Lag Measurements

[18] The results of our epoch and time lag measurements are shown in Table 2. Agreement between OC and SC values of the epochs of correlation maxima is generally excellent, with a root-mean square (RMS) deviation of 0.45 s. The largest discrepancy occurs for the 120314 data set with a 1.3 s difference.

[19] For the 100102 data set, reception of radar echoes started while the high correlation condition was already underway, and we were not able to measure the peak of the correlation maximum. We were able to secure an instantaneous spin rate estimate from repeated measurements during the second half of the high correlation period. Therefore, this data set was used for the determination of the instantaneous spin rate but not of the spin axis orientation.

[20] For reasons that are not entirely understood, we experienced considerable difficulties fitting for the epoch of correlation maximum to the 090113 and 090114 data sets. Differences of up to 6 s in the correlation maximum were obtained for various combinations of parameters (start times and integration times), and we declared these data sets

unsuitable for epoch measurements. However, we were able to use these data sets for time lag measurements.

[21] We performed spin orientation fits that excluded the 120314 measurements because of the 1.3 s discrepancy between OC and SC estimates of the epoch of correlation maximum. Analysis suggests that the OC value (MJD 56000.99151150) is inferior to the SC value (MJD 56000.99149649): removing the OC data point typically improves the goodness of fit by a factor of ∼3, whereas removing the SC data point has no substantial effect on the reduced χ^2 value. Despite the preference for the SC value of epoch t, we report the time lag measurement τ at the OC epoch for consistency with all other runs, and because doing so has no impact on the spin rate fits.

3.3. Spin Axis Orientation

[22] The spin axis orientation fits indicate that we can determine the epochs of correlation maxima to much better precision than the widths of the correlation function listed in Table 2. We assigned uncertainties to the epoch measurements corresponding to these widths divided by 10.

[23] Attempts to correct for atmospheric refraction by using fictitious observatory heights in the spin axis orientation fits only marginally improved the goodness of fit. Instead, we chose to solve for the spin axis orientation with various subsets of the data, including subsets only with data obtained at low zenith angle z, as these data are minimally affected by refraction. The 12 high-z epochs that were discarded can be easily identified in Table 1 as those with $\delta > 0.1$.

[24] Results of our spin axis orientation fits for various subsets of data are shown in Table 3, with the adopted best-fit obliquity of 2.04 arc min shown with an asterisk. The OC estimates are generally preferred because the OC SNR is ∼6 times higher than the SC SNR (Table 2), and because they generally provide a better fit to the data. Our assignment of uncertainties (0.08 arc min or 5 arc sec, one standard deviation) is guided by the range of values obtained for various subsets of data.

[25] Post-fit residuals are shown in Figure 2. We experimented with removing either or both largest residuals (080706 and 100110), but this did not affect the obliquity solution.

[26] The best-fit spin axis orientation at epoch J2000 is at equatorial coordinates (281.0103°, 61.4155°) and ecliptic coordinates (318.2352°, 82.9631°) in the corresponding J2000 frames (Figures 3 and 4). The discrepancy of 0.08 arc min compared with our previous estimate [Margot et al., 2007] can be attributed to additional data and improvements in analysis procedures. Whereas the 2007 estimate closely matched the predicted location of Cassini state 1, our current best-fit value places the pole 2.7 arc sec away from the Cassini state. There are several possible interpretations: 1) given the 5 arc sec uncertainty on spin axis orientation, Mercury may in fact be in the exact Cassini state, 2) Mercury may also be in the exact Cassini state if our knowledge of the location of that state is imprecise, which is possible because it is difficult to determine the exact Laplacian pole orientation, 3) Mercury may lag the exact Cassini state by a few arc sec, 4) Mercury may lead the exact Cassini state, although this seems less likely based on the evidence at hand. Measurement of the offset between the

Table 2. Log of Observations[a]

No.	Date (yymmdd)	t (MJD)	w (s)	w' (s)	τ (s)	σ (10^{-5})	Spin ($3/2n$)	μ_c
01	020513	52407.88968000	4.41	1.36	−12.36951	2.13	0.999991	0.176
02	020522	52416.87125769	6.27	1.60	−12.69226	1.58	0.999885	0.157
03	020602	52427.84553877	5.98	1.31	−11.84074	1.69	0.999865	0.156
04	020612	52437.81605188	6.35	1.87	−11.21226	1.78	0.999945	0.170
05	030113	52652.76020509	10.32	2.84	−10.93557	1.40	1.000106	0.154
06	030123	52662.72579134	8.40	3.33	−11.29543	1.17	1.000069	0.149
07	030531	52790.84692546	7.76	2.66	−8.30669	1.49	0.999938	0.160
08	030601	52791.84416437	7.37	2.63	−8.36902	0.88	0.999954	0.145
09	040331	53095.96834568	5.92	2.26	−7.41569	1.45	1.000110	0.165
10	041212	53351.86633414	7.86	2.87	−7.74050	1.75	1.000098	0.163
11	041218	53357.84852119	7.75	3.33	−7.38328	1.56	1.000086	0.158
12	041219	53358.84540081	8.13	3.67	−7.39328	3.25	1.000103	0.157
13	050314	53443.00432021	7.04	3.23	−4.78478	4.84	1.000110	0.173
14	050315	53444.00109429	6.87	2.76	−4.98779	3.36	1.000097	0.167
15	050316	53445.99476137	6.72	2.44	−5.31603	2.29	1.000082	0.170
16	050318	53447.98862140	6.24	2.99	−5.53563	2.81	1.000079	0.174
17	060629	53915.73546725	8.03	2.23	−11.27626	1.01	0.999868	0.190
18	060712	53928.67664070	7.94	1.71	−10.71487	0.88	0.999889	0.183
19	080705	54652.73041514	9.53	4.52	−11.82003	2.04	1.000077	0.137
20	080706	54653.72649362	10.48	4.91	−11.73815	1.10	1.000077	0.146
21	090112	54843.75831952	7.53	3.99	−10.51817	1.49	1.000093	0.216
22	090113	54844.75437248	-	-	−10.50081	1.92	1.000080	0.177
23	090114	54845.75045821	-	-	−10.49273	1.29	1.000081	0.175
24	090619	55001.78844629	9.15	4.06	−10.43065	2.08	1.000062	0.145
25	100102	55198.80132020	-	-	−10.60219	1.15	1.000087	0.176
26	100103	55199.79795657	9.67	2.82	−10.57556	1.80	1.000090	0.182
27	100110	55206.77348354	9.00	2.78	−10.64920	1.40	1.000103	0.164
28	110415	55666.93282866	4.25	1.03	−5.17857	2.53	0.999925	0.175
29	110416	55667.93116893	4.78	1.61	−4.98768	2.55	0.999881	0.167
30	120313	55999.99459676	4.36	1.65	−4.55569	4.07	1.000086	0.172
31	120314	56000.99151150	3.33	1.07	−4.54802	10.2	1.000147	0.175
32	120315	56001.98848792	5.24	1.60	−4.51185	2.68	1.000078	0.177
33	120702	56110.72192047	7.93	2.34	−9.44909	1.31	0.999905	0.186
34	120703	56111.71729265	7.83	2.38	−9.30992	2.86	0.999891	0.198
35	120704	56112.71260442	7.51	2.73	−9.16507	1.92	0.999891	0.186

[a]The epoch of speckle correlation maximum t is the centroid of a Gaussian of standard deviation w and reported as a Modified Julian Date (MJD). The w' values have been scaled by $1/\sqrt{SNR}$ (Appendix A). The time lag τ indicates the time interval for speckles to travel from one station to the other at the corresponding epoch. The reference epochs correspond to arrival times at Goldstone, and the negative lag values indicate that Mercury speckles travel from east to west. The fractional uncertainty σ in the time lag and spin rate is empirically determined from successive measurements, except in the first four data sets where it corresponds to a residual timing uncertainty of 0.2 ms. The penultimate column indicates the instantaneous spin rate in units of $3/2$ the mean orbital frequency, with the refraction corrections listed in Table 1 applied. The last column shows the circular polarization ratio, i.e., the ratio of SC echo power to OC echo power. OC values are shown; SC values are available upon request.

spin axis orientation and the exact Cassini state location is important, as it can potentially place bounds on energy dissipation due to solid-body tides and core-mantle interactions [*Yoder*, 1981; *Williams et al.*, 2001]. S. J. Peale et al. (Dissipative offset of Mercury's spin axis from Cassini state 1, manuscript in preparation, 2012) examine the magnitude of the offset for various core-mantle coupling mechanisms.

3.4. Amplitude of Longitude Libration

[27] The observed instantaneous spin rates (Table 2) reveal an obvious forced libration signature with a period of 88 days (Figure 5). One can fit a libration model [*Margot*,

Table 3. Results of Spin Axis Orientation Fits[a]

Pol	N	θ_w	χ_ν^2	$\theta_{w'}$	χ_ν^2	Notes
OC	32	2.092	1.02	2.083	9.29	
OC	31	2.057	0.43	2.047	3.25	120314 removed
OC[*]	20	2.042	0.12	2.042	1.09	low-z subset
SC	32	2.085	1.11	2.077	1.89	
SC	31	2.084	1.14	2.074	1.94	120314 removed
SC	20	2.094	0.54	2.093	1.02	low-z subset
XC	64	2.087	1.03	2.081	5.40	
XC	62	2.076	0.77	2.055	2.56	120314 removed
XC	40	2.079	0.35	2.058	1.17	low-z subset

[a]The first and second columns indicate the polarization (OC, SC, or both) and the number N of independent data points used in the fit. The obliquity values determined for natural scaling and SNR scaling are shown as θ_w and $\theta_{w'}$, respectively, with the associated reduced χ^2 values. The χ^2 values are computed on the basis of the widths w and w' (Table 2) divided by 10. The best-fit and adopted obliquity value is shown with an asterisk.
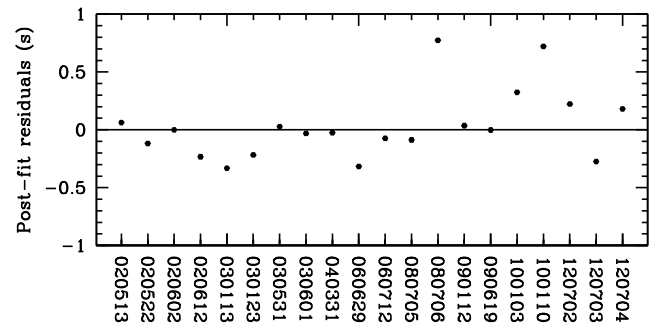
Figure 2. Post-fit residuals, in seconds, from the adopted spin axis orientation fit (20 OC epochs).
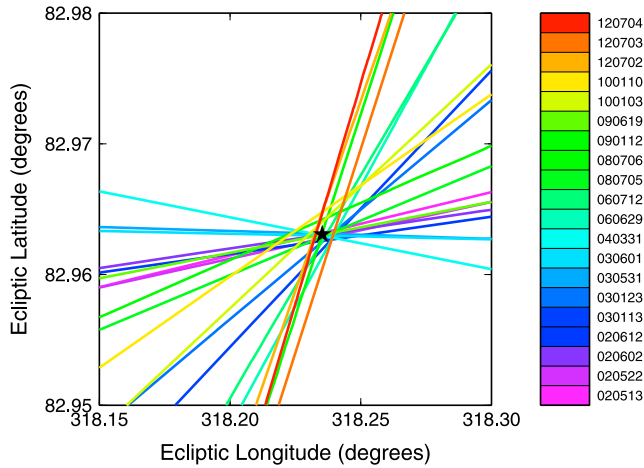
Figure 3. Constraints on spin axis orientation from 20 epochs of correlation maxima observed at low zenith angles (subset identified with an asterisk in Table 3). Epochs are color-coded according to the scale bar at right. The orientation of each line is dictated by the ecliptic longitude of the projected baseline at the corresponding epoch. The individual constraints appear as lines on the celestial sphere because a rotation of the spin vector of Mercury about an axis parallel to the projected baseline does not result in a substantial change in the epoch of correlation maximum. Observations at a range of baseline geometries determine the spin axis orientation in two dimensions. The best-fit spin-axis orientation is marked with a star.

2009] to the data and derive the value of $(B - A)/C_m$. Adjusting for the amplitude of the libration in a least-squares sense, we obtain a very good fit ($\chi^2_\nu = 0.40$) with a best-fit value of $(B - A)/C_m = (2.18 \pm 0.09) \times 10^{-4}$, where the adopted one-sigma uncertainty represents twice the formal uncertainty of the fit. This amounts to a libration amplitude of (38.5 ± 1.6) arc sec, or a longitudinal displacement of 450 meters at the equator.

[28] Post-fit residuals of the spin rate data with respect to the libration model are shown in Figure 6. The apparent structure in residuals at low orbital phases may indicate a deficiency in the libration model, but is not expected to substantially affect the overall libration amplitude.

[29] More elaborate libration models can be considered, but they do not change our conclusions. First, we fit the data to a three-parameter model that allows for a free libration component of period $[3(B - A)/(C_m)(7e/2 - 123e^3/16)]^{-1/2}$ times the orbital period, or ~4257 days. The three parameters are the overall libration amplitude, initial libration angle γ_0, and initial angular velocity $(d\gamma/dt)_0$, where we chose the 2002 April 17 perihelion passage (MJD 52381.480) as the initial epoch. The best-fit values are $(B - A)/C_m = 2.19 \times 10^{-4}$, $\gamma_0 = 33$ arc sec, and $(d\gamma/dt)_0 = 2.13$ arc sec/day, with a goodness of fit ($\chi^2_\nu = 0.39$) that is only marginally better than our single-parameter model. Because this model does not provide a significant improvement, and because the formal uncertainties on γ_0 and $(d\gamma/dt)_0$ are comparable to the best-fit values themselves, it is dubious whether a free libration is detected and whether the best-fit values of γ_0 and $(d\gamma/dt)_0$

have any meaning. Second, we fit the spin data to a model that takes into account long-period librations forced by other planets, as described by *Peale et al.* [2007, 2009] and *Yseboodt et al.* [2010]. We find a comparable goodness of fit ($\chi^2_\nu = 0.41$) and a similar value of $(B - A)/C_m = 2.20 \times 10^{-4}$. Because of the proximity to a resonance with Jupiter's orbital period, this model can in principle be used to assign tighter error bars on $(B - A)/C_m$. The corresponding one-sigma uncertainty, taken again as twice the formal uncertainty of the fit, would be 0.06×10^{-4}.

[30] An independent, spacecraft-based measurement of the forced libration amplitude was recently provided by A. Stark et al. (A technique for measurements of physical librations from orbiting spacecraft: Application to Mercury, paper to be presented at European Planetary Science Congress, Madrid, 23–28 September 2012). Their value (36.5 ± 3.2 arc sec) is consistent with our best-fit estimate.

4. Interior Structure

[31] Our obliquity measurement [$\theta = (2.04 \pm 0.08)$ arc min] and libration amplitude measurement [$(B - A)/C_m = (2.18 \pm 0.09) \times 10^{-4}$] can be combined with gravitational harmonics [*Smith et al.*, 2012] to infer the value of Mercury's MoI and that of its outer shell. Values of Mercury's orbital precession rate and orbital inclination with respect to the Laplace plane ι are needed for this calculation. We use the values determined by *Yseboodt and Margot* [2006]:
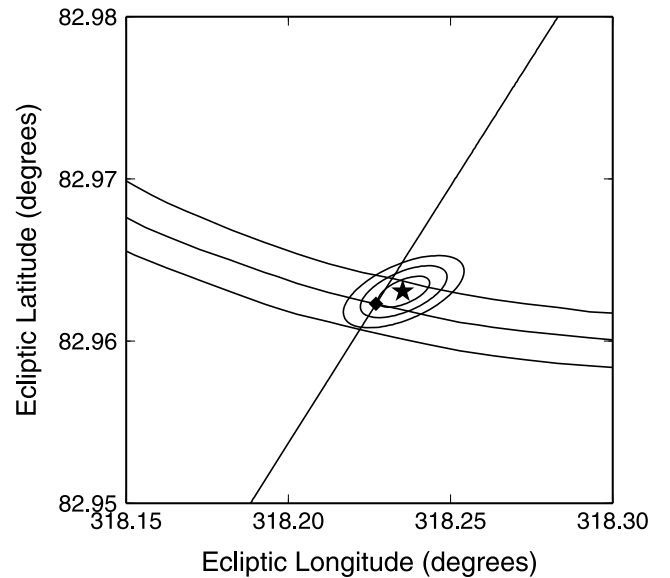

Figure 4. Orientation of the spin axis of Mercury obtained by a least-squares fit to a subset of epochs that are minimally affected by atmospheric refraction. Contours representing 1-, 2-, and 3-σ uncertainty regions surrounding the best-fit solution (star) are shown. The contours are elongated along the general direction of the constraints shown in Figure 3. The best-fit obliquity is (2.04 ± 0.08) arc min. The diamond and curved lines show the solution and obliquity uncertainties of *Margot et al.* [2007]. The oblique line shows the predicted location of Cassini state 1 based on the analysis of *Yseboodt and Margot* [2006].
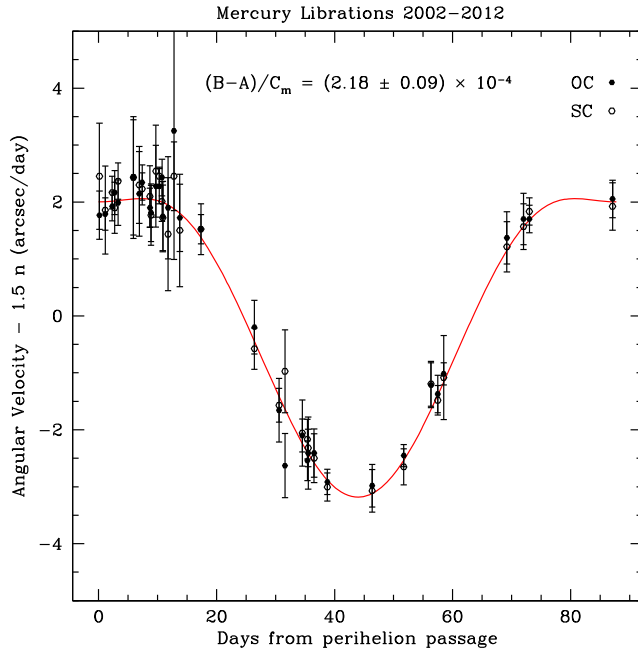
Figure 5. Mercury librations revealed by 35 OC and SC instantaneous spin rate measurements obtained between 2002 and 2012. The measurements with their one-standard-deviation errors are shown in black. A numerical integration of the torque equation is shown in red. The flat top on the angular velocity curve near pericenter is due to the momentary retrograde motion of the Sun in the body-fixed frame and corresponding changes in the torque. The amplitude of the libration curve is determined by a one-parameter least-squares fit to the observations, which yields a value of $(B - A)/C_m = (2.18 \pm 0.09) \times 10^{-4}$ with reduced χ^2 of 0.4.

precession period of 328,000 years and $\iota = 8.6°$. For J_2 and C_{22} we used the values 5.031×10^{-5} and 0.809×10^{-5}, with 0.4% and 0.8% uncertainties, respectively [*Smith et al.*, 2012].

[32] In order to propagate errors on all four key parameters $(\theta, (B - A)/C_m, C_{20}, C_{22})$ we perform Monte-Carlo simulations in which 100,000 Gaussian deviates of the quantities are obtained from their nominal values and one-standard-deviation errors.

[33] We first use equation 12 of *Yseboodt and Margot* [2006], which is an explicit version of equation (2), to estimate Mercury's polar MoI $C/MR^2 = 0.346 \pm 0.014$ (Figure 7). We then use equation (3) to estimate the fraction corresponding to the outer librating shell $C_m/C = 0.431 \pm 0.025$ (Figure 8). Finally, we combine these two values to arrive at the outer shell MoI $C_m/MR^2 = 0.149 \pm 0.006$ (Figure 9). Because these values depend on the radial distribution of mass in the interior, they represent important boundary conditions that models of the interior of Mercury must satisfy. The MoI values can be used to estimate the size of the core of Mercury.

[34] Consider a simple two-layer model with a core of uniform density ρ_c and radius R_c and a mantle of uniform density ρ_m extending from R_c to the radius of the planet $R = 2440$ km. One can write three equations in the three unknowns R_c, ρ_c, and ρ_m that must satisfy the C/MR^2 and
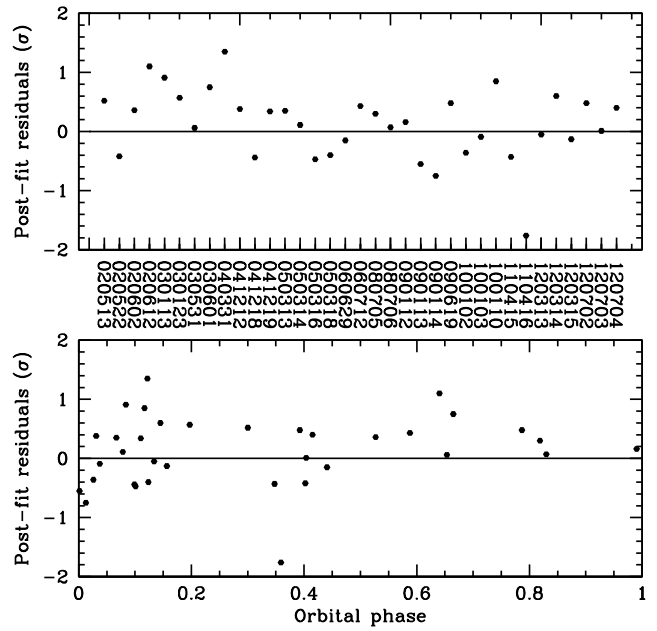

Figure 6. OC post-fit residuals from the one-parameter libration fit shown as a function of (top) observing date and (bottom) orbital phase, where 0 and 1 mark pericenter. Each residual is the observed minus computed quantity, divided by the corresponding measurement uncertainty.

C_m/C constraints above as well as the total mass of Mercury $M = 4\pi R^3 \bar{\rho}/3$, where $\bar{\rho} = 5428$ kg/m^3 is the mean density of Mercury. The solution gives a core radius $R_c = 1998$ km, or 82% of the radius of the planet, with densities of core and
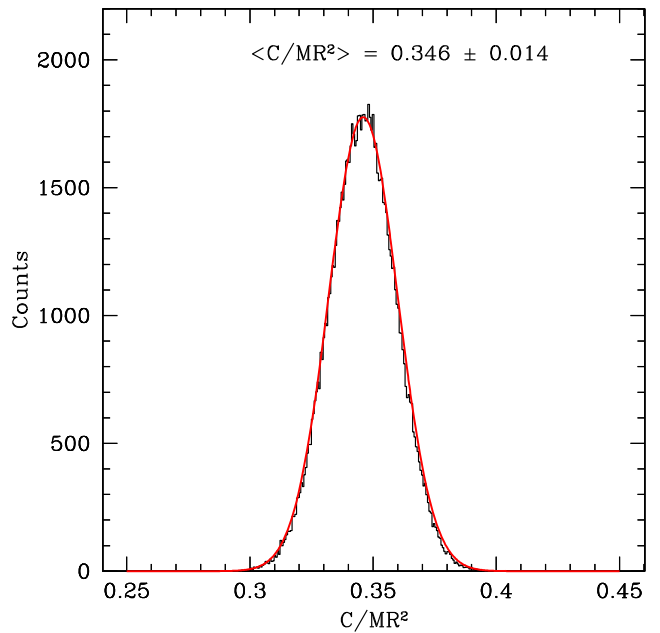

Figure 7. Distribution of C/MR^2 values from 100,000 Monte Carlo trials that capture uncertainties in obliquity, libration amplitude, and gravitational harmonics. C is the moment of inertia of Mercury.
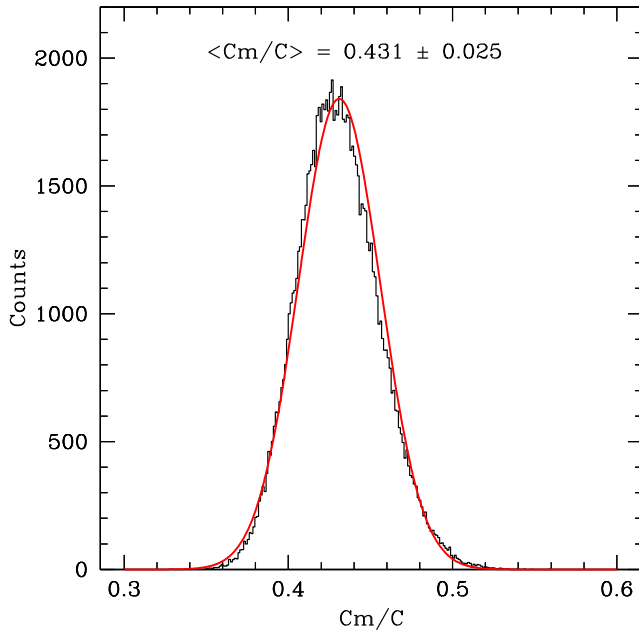
Figure 8. Distribution of C_m/C values from 100,000 Monte Carlo trials that capture uncertainties in obliquity, libration amplitude, and gravitational harmonics. C_m/C is the fraction of the moment of inertia that corresponds to the outer librating shell.

Figure 9. Distribution of C_m/MR^2 values from 100,000 Monte Carlo trials that capture uncertainties in obliquity, libration amplitude, and gravitational harmonics. C_m is the moment of inertia of the outer librating shell. The moment of inertia of the core is $C_c = C - C_m$.

mantle material of $\rho_c = 1.3365\bar{\rho} = 7254$ kg/m^3 and $\rho_m = 0.5902\bar{\rho} = 3203$ kg/m^3. For interior models that are more elaborate and realistic, see S. A. Hauck, et al. (The curious case of Mercury's internal structure, manuscript in preparation, 2012).

[35] Our formalism for inferring C_m/C relies on the assumption that both the core-mantle boundary (CMB), and inner core boundary (ICB), if present, are axially symmetric. However a distortion of the CMB is almost certainly present due to the asymmetry in the mantle and possible fossil signatures of convective or tidal processes. P. Gao and D. J. Stevenson (The effect of nonhydrostatic features on the interpretation of Mercury's mantle density from Messenger results, paper to be presented at the Division for Planetary Sciences Annual Meeting, Reno, Nevada, 14–19 October 2012) compute the core contribution to the overall (B-A), assuming that the CMB is an equipotential, and suggest that it can affect inferences on mantle density by 10–20%. Although the exact effect of the core contribution is still an active area of research, it would be prudent to exercise some caution when interpreting the spin and gravity data in terms of interior properties. Because the geometry and coupling at the CMB and ICB affect the short-term and long-term rotational behavior of the planet, rotational data provide the interesting prospect of placing bounds on these quantities [*Rambaux et al.*, 2007; *Veasey and Dumberry*, 2011; *Dumberry*, 2011; *Van Hoolst et al.*, 2012; Peale et al., in preparation, 2012].

5. Conclusions

[36] Earth-based radar observations of Mercury spanning 10 years yield estimates of spin state quantities which, in
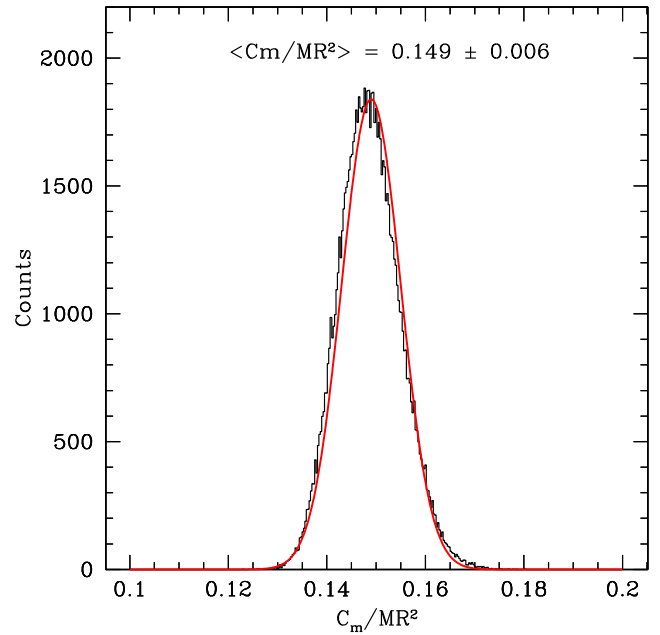
combination with second-degree gravitational harmonics [*Smith et al.*, 2012] and the formalism of *Peale* [1976], provide the moment of inertia of the innermost planet.

Appendix A: Correlation Estimates

[37] After conversion to baseband, the signals are sampled in-phase (I) and quadrature (Q), such that the I and Q samples can be thought of as the real and imaginary parts of a complex signal $\{z(t)\}$, with $z(t) = I(t) + jQ(t)$ and $j = \sqrt{-1}$.

[38] The complex-valued cross-correlation of the signals $\{z_1(t)\}$ and $\{z_2(t)\}$ is given by

$$R_{z_1 z_2}(\tau) = E\big[z_1(t)z_2^*(t+\tau)\big], \qquad (A1)$$

where E[] represents the expectation value operator, and * represents the complex conjugate operator. The normalized value of the correlation is obtained with

$$\rho_{z_1 z_2}(\tau) = \frac{|R_{z_1 z_2}(\tau)|}{\sqrt{|R_{z_1 z_1}(0)R_{z_2 z_2}(0)|}}, \qquad (A2)$$

where $\|$ is the absolute value operator. Since the maximum possible value of the correlation $R_{zz}(\tau)$ occurs at $\tau = 0$, $\rho_{z_1 z_2}(\tau)$ is ≤ 1 for all τ.

[39] The expectation value of an estimate $\hat{\phi}$ of a quantity ϕ is given by

$$E\big[\hat{\phi}\big] = \lim_{N\to\infty} \frac{1}{N}\sum_{i=1}^{N}\hat{\phi}_i. \qquad (A3)$$

The number of samples N that we use in our calculations is given by the product of the sample rate f_s or bandwidth B

(in Hertz) and the duration T (in seconds). If the signals $\{z_1(t)\}$ and $\{z_2(t)\}$ are uncorrelated, one can show that $E[\rho_{z_1 z_2}(\tau)] = 1/\sqrt{BT}$ for all τ.

[40] In the radar speckle displacement situation, the radar echoes received at two telescopes are well described by $z_1(t) = s(t) + m(t)$ and $z_2(t) = s(t - \tau) + n(t)$, where $s(t)$ is the common speckle signal, $m(t)$ and $n(t)$ are noise contributions, τ is a time lag dictated by the orbital and spin motions, and $s(t)$, $m(t)$, and $n(t)$ are uncorrelated. The zero-lag value of the auto-correlation of the signal at antenna 1 is

$$R_{z_1 z_1}(0) = R_{ss}(0) + R_{mm}(0) = S + M, \qquad (A4)$$

where S is the signal power and M is the noise power at antenna 1, with an equivalent expression for antenna 2.

[41] In our analysis we seek to obtain an estimate $\hat{\tau}$ of the time lag by cross-correlating the signals received at both antennas and by measuring the location of the peak of the correlation function. Uncertainties on the location of the peak of a cross-correlation function $R_{z_1 z_2}(\tau)$ are assigned on the basis of a development derived by *Bendat and Piersol* [2000]. They show that if the correlation function near its peak has the form associated with bandwidth-limited white noise, i.e.,

$$\rho_{z_1 z_2}(\tau) = \rho_{z_1 z_2}(0) \frac{\sin 2\pi B\tau}{2\pi B\tau}, \qquad (A5)$$

then the one-standard-deviation uncertainty on τ is given by

$$\sigma_1(\tau) = \frac{(3/4)^{1/4}}{\pi B} \left\{ \frac{2 + (M/S) + (N/S) + (M/S)(N/S)}{2BT} \right\}^{1/4} \qquad (A6)$$

We use a similar form appropriate for a correlation function that is Gaussian near its peak,

$$\sigma_1(\tau) = (4/3)^{1/4} \sigma \{\cdots\}^{1/4}, \qquad (A7)$$

where σ is the characteristic width of the Gaussian and the expression within curly braces is unchanged. In the high-SNR limit, this reduces to

$$\sigma_1(\tau) \simeq (4/3)^{1/4} \sigma \{1/BT\}^{1/4} \propto \frac{\sigma}{\sqrt{\text{SNR}}}, \qquad (A8)$$

since the SNR is proportional to $\sqrt{BT}$.

Appendix B: Formalism for Computing Correlation Conditions

[42] *Holin* [1988, 1992] described the conditions for high correlation in the speckle displacement problem. He developed approximate vectorial expressions describing the spin-orbital geometry. Although useful to guide intuition and understanding, the approximate expressions cannot be used to plan or interpret actual observations. Here we describe the formalism used for our observations, and for similar observations of Venus and Galilean satellites.

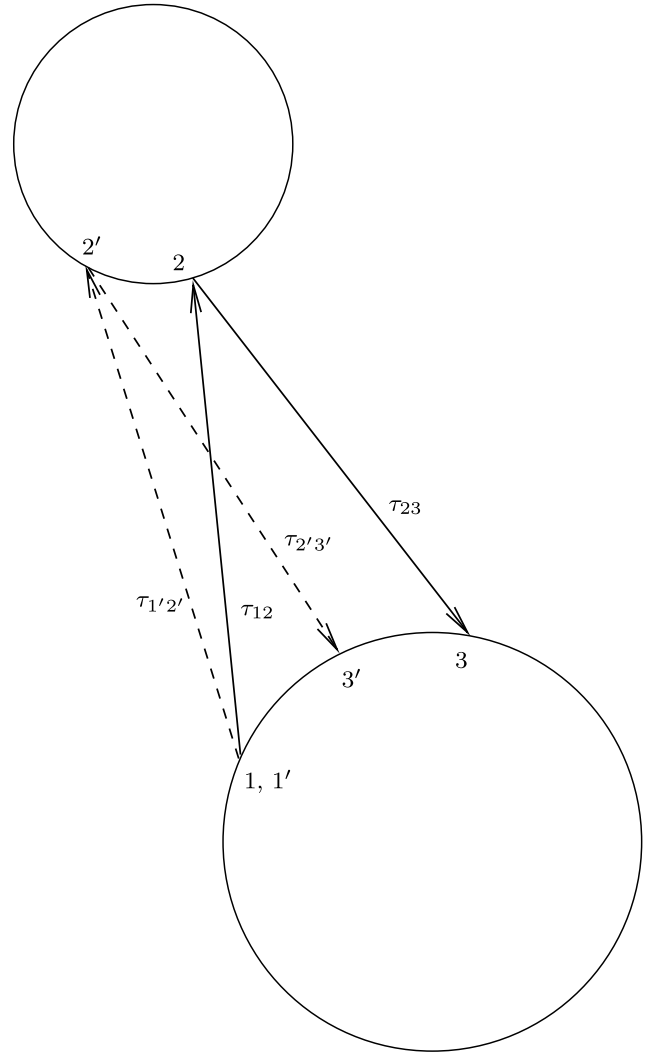[43] The geometry of the speckle displacement problem involves three radio observatories, six epochs of participation

Figure B1. The geometry of the speckle displacement problem involves one transmit station (1 and 1′), two receive stations (3 and 3′), six epochs of participation (two transmit epochs, two bounce epochs, two receive epochs), and four light-time quantities (τ_{ij}). For simplicity, the substantial spin and orbital motions of the planets that occur between the first transmit epoch and the last receive epoch are not shown.

(two transmit epochs, two bounce epochs, two receive epochs), and four light-time quantities (Figure B1). The transmit site is identified with the numbers 1 and 1′; the bounce sites are identified with the numbers 2 and 2′, and the receive sites are identified with the numbers 3 and 3′, where the unprimed quantities refer to one transmit-receive antenna pair and the primed quantities refer to the other transmit-receive antenna pair. In our observations the transmit antenna also serves as one of the receive antennas, reducing the number of telescopes from three to two.

[44] Maximum correlation between the two echo time series occurs when the speckles observed by station 3 at its receive epoch are most similar to speckles observed by station 3′ at its receive epoch. This condition depends on the spin and orbital states of the Earth and target at all epochs of

participation in the upleg-bounce-downleg sequence. During the planning stages we predict high-correlation conditions by minimizing an angular distance criterion involving the upleg and downleg vectors relevant to each pair of transmit-receive antennas. During the data analysis stages we adjust the spin state variables so that the predictions give the best match to observations.

[45] Reflection of electromagnetic waves at a moving interface must be treated according to the prescriptions of special relativity [*Einstein*, 1905]. Specifically one ought to perform Lorentz transformations to a frame in which the boundary is at rest before applying the laws of reflection. We consider three space-time coordinate systems moving with respect to one another. One is a frame centered on the solar system barycenter (SSB); the other two are frames in which the vacuum-surface boundary at the bounce points is at rest at the relevant bounce epochs. We compute the appropriate relative velocities between these frames and apply Lorentz transformations to the four-vectors representing the upleg and downleg electromagnetic waves (frequency and wave number vector).

[46] In our formalism, the state vector (position and velocity) in the SSB frame for site i ($i = 1, 1', 2, 2', 3, 3'$) at its epoch of participation is given by $(\mathbf{r_i}, \dot{\mathbf{r}_i})$. Light times between sites i and $j \neq i$ ($j = 1, 1', 2, 2', 3, 3'$) are computed to first order by forming the vectorial difference $\mathbf{r_{ij}} = \mathbf{r_j} - \mathbf{r_i}$ and dividing its norm by the speed of light; $\tau_{ij} = \mathbf{r_{ij}}/c$. General relativistic corrections to the light times are computed according to the formalism of *Moyer* [1971]. The epochs of participation expressed in barycentric dynamical time are t_3 and $t_{3'}$ (receive), $t_2 = t_3 - \tau_{23}$ and $t_{2'} = t_{3'} - \tau_{2'3'}$ (bounce), and $t_1 = t_3 - \tau_{23} - \tau_{12}$ and $t_{1'} = t_{3'} - \tau_{2'3'} - \tau_{1'2'}$ (transmit). The epoch of correlation maximum is reported as that time t_3 at which maximum correlation is observed, and the corresponding time lag for maximum correlation is reported as $t_3 - t_{3'}$. All of these calculations are greatly facilitated by the use of the NAIF SPICE routines [*Acton*, 1996].

Appendix C: Refraction Corrections

[47] The observer is located at O, at a distance $r_0 = \overline{CO}$ from the center of Earth (Figure C1). The height of the atmosphere beyond which refraction effects are negligible is $H = \overline{OT}$. We consider a light ray that crosses this height at A′ and reaches the observer on the surface at O. The observed or apparent direction to the source is at a zenith angle z_0. The geometrical direction to the source is at a zenith angle $z_0 + \Delta z$, where Δz represents the total bending of light. The bending of light in a spherically symmetric atmosphere is determined by applying Snell's law in spherical coordinates $nr \sin z = $ constant [*Smart*, 1962], where n is the index of refraction. Writing the equality at O and A′, we have

$$n_0 r_0 \sin z_0 = (r_0 + H) \sin z \qquad (C1)$$

since $n = 1$ in vacuum. The quantities of interest are the distance $\overline{AB}$ between the refracted light ray and the unrefracted path, and its projection $\overline{OP}$ along the zenith direction. These cause a change in the apparent position of the antenna and
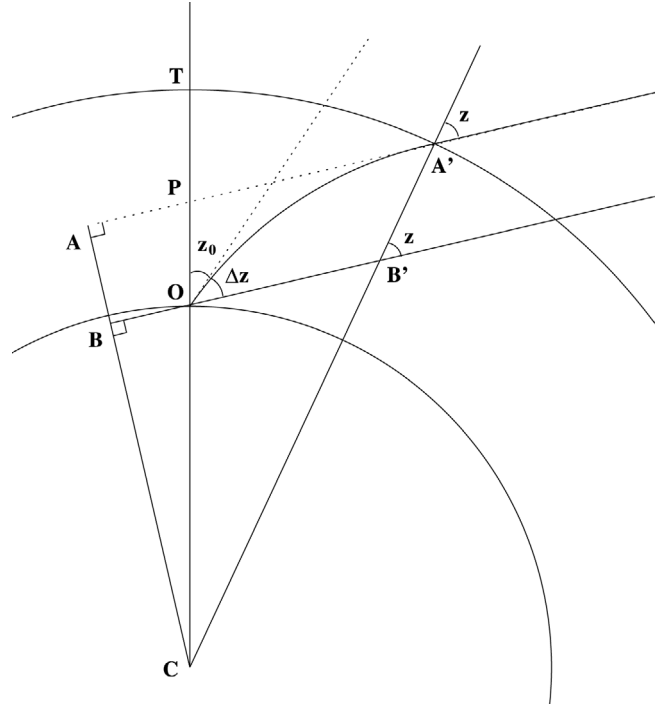

Figure C1. Geometry for atmospheric refraction calculations (see text).

therefore modify the effective baseline length. We compute $\overline{AB}$ and $\overline{OP}$ by solving the following equations:

$$\overline{OP} = \overline{AB} / \sin(z_0 + \Delta z), \qquad (C2)$$

$$\overline{AB} = \overline{AC} - \overline{BC}, \qquad (C3)$$

$$\overline{AC} = (r_0 + H) \sin z, \qquad (C4)$$

$$\overline{BC} = r_0 \sin(z_0 + \Delta z). \qquad (C5)$$

The computations of n_0 and Δz require integrations through a model atmosphere; we used the formalism described in the Explanatory Supplement to the Astronomical Almanac [*Seidelmann*, 1992] with a tropopause height of 11 km, a temperature lapse rate of 6.5 K/km in the troposphere, and $H = 80$ km. In principle the calculations depend on atmospheric conditions (pressure, temperature, relative humidity), but we found that standard conditions (P = 101325 Pa, T = 273.15 K, zero relative humidity) provide excellent corrections.

References

Acton, C. H. (1996), Ancillary data services of NASA's Navigation and Ancillary Information Facility, *Planet. Space Sci.*, *44*, 65–70.

Bendat, J. S., and A. G. Piersol (2000), *Random Data Analysis and Measurement Procedures*, 3rd ed., Wiley, Hoboken, N. J.

Dumberry, M. (2011), The free librations of Mercury and the size of its inner core, *Geophys. Res. Lett.*, *38*, L16202, doi:10.1029/2011GL048277.

Einstein, A. (1905), Zur Elektrodynamik bewegter Körper, *Ann. Phys.*, *322*, 891–921.

Folkner, W. M., J. G. Williams, and D. H. Boggs (2008), JPL Planetary Ephemeris DE 421, *Tech. Rep. IOM 343R-08-003*, Jet Propul. Lab., Pasadena, Calif.

Hauck, S. A., S. C. Solomon, and D. A. Smith (2007), Predicted recovery of Mercury's internal structure by MESSENGER, *Geophys. Res. Lett.*, *34*, L18201, doi:10.1029/2007GL030793.

Holin, I. V. (1988), Spatial-temporal coherence of a signal diffusely scattered by an arbitrarily moving surface for the case of monochromatic illumination [in Russian], *Izv. Vyssh. Uchebn. Zaved. Radiofiz.*, *31*, 515–518. [*Radiophys. Quant. Elec.*, Engl. Transl., *31*, 371–374.]

Holin, I. V. (1992), Accuracy of body-rotation-parameter measurement with monochromomatic illumination and two-element reception [in Russian], *Izv. Vyssh. Uchebn. Zaved. Radiofiz.*, *35*, 433–439. [*Radiophys. Quant. Elec.*, Engl. Transl., *35*, 284–287.]

Konopliv, A. S., S. W. Asmar, W. M. Folkner, Ö. Karatekin, D. C. Nunes, S. E. Smrekar, C. F. Yoder, and M. T. Zuber (2011), Mars high resolution gravity fields from MRO, Mars seasonal gravity, and other dynamical parameters, *Icarus*, *211*, 401–428.

Margot, J.-L. (2009), A Mercury orientation model including non-zero obliquity and librations, *Celest. Mech. Dyn. Astron.*, *105*, 329–336.

Margot, J.-L., S. J. Peale, R. F. Jurgens, M. A. Slade, and I. V. Holin (2007), Large longitude libration of Mercury reveals a molten core, *Science*, *316*, 710–714.

Moyer, T. D. (1971), Mathematical formulation of the Double-Precision Orbit Determination Program (DPODP), *Tech. Rep. 32–1527*, Jet Propul. Lab., Pasadena, Calif.

Peale, S. J. (1969), Generalized Cassini's laws, *Astron. J.*, *74*, 483–489.

Peale, S. J. (1976), Does Mercury have a molten core?, *Nature*, *262*, 765–766.

Peale, S. J. (1988), The rotational dynamics of Mercury and the state of its core, in *Mercury*, edited by F. Vilas, C. R. Chapman, and M. S. Matthews, pp. 461–493, Univ. of Ariz. Press, Tucson.

Peale, S. J., M. Yseboodt, and J.-L. Margot (2007), Long-period forcing of Mercury's libration in longitude, *Icarus*, *187*, 365–373.

Peale, S. J., J.-L. Margot, and M. Yseboodt (2009), Resonant forcing of Mercury's libration in longitude, *Icarus*, *199*, 1–8.

Rambaux, N., T. van Hoolst, V. Dehant, and E. Bois (2007), Inertial core-mantle coupling and libration of Mercury, *Astron. Astrophys.*, *468*, 711–719, doi:10.1051/0004-6361:20053974.

Riner, M. A., C. R. Bina, M. S. Robinson, and S. J. Desch (2008), Internal structure of Mercury: Implications of a molten core, *J. Geophys. Res.*, *113*, E08013, doi:10.1029/2007JE002993.

Rivoldini, A., T. van Hoolst, and O. Verhoeven (2009), The interior structure of Mercury and its core sulfur content, *Icarus*, *201*, 12–30.

Seidelmann, P. K. (Ed.) (1992), *Explanatory Supplement to the Astronomical Almanac*, Univ. Sci. Books, Sausalito, Calif.

Smart, W. (1962), *Textbook on Spherical Astronomy*, Cambridge Univ. Press, Cambridge, U. K.

Smith, D. E., et al. (2012), Gravity field and internal structure of Mercury from MESSENGER, *Science*, *336*, 214–217.

Van Hoolst, T., A. Rivoldini, R.-M. Baland, and M. Yseboodt (2012), The effect of tides and an inner core on the forced longitudinal libration of Mercury, *Earth Planet. Sci. Lett.*, *333*, 83–90, doi:10.1016/j.epsl.2012.04.014.

Veasey, M., and M. Dumberry (2011), The influence of Mercury's inner core on its physical libration, *Icarus*, *214*, 265–274, doi:10.1016/j.icarus.2011.04.025.

Williams, J. G., D. H. Boggs, C. F. Yoder, J. T. Ratcliff, and J. O. Dickey (2001), Lunar rotational dissipation in solid body and molten core, *J. Geophys. Res.*, *106*, 27,933–27,968.

Yoder, C. F. (1981), The free librations of a dissipative moon, *Philos. Trans. R. Soc. London A*, *303*, 327–338.

Yoder, C. F. (1995), Astrometric and geodetic properties of Earth and the solar system, in *Global Earth Physics: A Handbook of Physical Constants*, *AGU Ref. Shelf*, vol. 1, edited by T. J. Ahrens, pp. 1–31, AGU, Washington, D. C., doi:10.1029/RF001p0001.

Yseboodt, M., and J.-L. Margot (2006), Evolution of Mercury's obliquity, *Icarus*, *181*, 327–337.

Yseboodt, M., J. Margot, and S. J. Peale (2010), Analytical model of the long-period forced longitude librations of Mercury, *Icarus*, *207*, 536–544.